https://doi.org/10.5194/egusphere-2025-3880
Preprint. Discussion started: 15 December 2025

Earth system modelling of mercury using CESM2 – Part 3: Oceanic model POP2/Hg v1.0

Mao Mao[1,2], Yujuan Wang[1], Peng Zhang[1], Ling Li[1], Shaojian Huang[1], Chen Zhou[1], Yanxu Zhang[2]

[1]School of Atmospheric Science, Nanjing University, Nanjing, 210003, China
[2]Earth & Environmental Sciences, Tulane University, New Orleans, 70118, the United States

Correspondence to: Yanxu Zhang (yzhang127@tulane.edu)

Abstract. Mercury (Hg) is a globally distributed toxicant with complex cycling in the ocean, involving redox reactions, air–sea exchange, and microbial methylation. We present POP2/Hg v1.0, a new global ocean mercury model developed within the ocean component of CESM2 (POP2) and coupled to the Marine Biogeochemistry Library (MARBL). POP2/Hg v1.0 simulates dissolved elemental Hg (Hg^0), oxidized Hg (Hg^{II}), particulate-bound Hg (Hg^p), and Methylmercury (MeHg = MMHg + DMHg), linking their transformation to ecosystem processes and dynamics of particulate organic carbon (POC). The model captures observed large-scale features of marine Hg. Surface Hg^0 concentrations range from 10 to 120 fmol L^{-1}(fM, 1 fM = 10^{-15} mol L^{-1}) and are elevated in tropical and subtropical oceans due to strong photoreduction and limited evasion. Subsurface Hg^0 maxima emerge in upwelling zones, reflecting remineralization-driven Hg^{II} reduction. Surface Hg^{II} concentrations peak in regions of high atmospheric deposition and productivity and rise at depth in oxygen-deficient zones. Hg^p is closely associated with high POC and Hg^{II} levels in the surface ocean but attenuates rapidly with depth due to remineralization. MeHg accumulates in the subsurface and deep sea, broadly consistent with observations. Total Hg (Hg^T) ranges to above 2.0 pmol L^{-1} (pM, 1 pM = 10^{-12} mol L^{-1}) in the surface, with open-ocean surface concentrations matching measurements. Deep-ocean Hg^T accumulation reflects sustained particle flux and remineralization. The biological pump strongly shapes vertical Hg transport. Above 1000 m, soft POC carries 98.6% of Hg^p flux, driving export and remineralization. Below 1000 m, hard POC becomes the dominant carrier, contributing over 99% of Hgp flux to sediments, although the total flux is small (0.19 t yr^{-1}). Sensitivity tests show that altering redox rates significantly affects the vertical distribution of Hg transformations. Reduced surface reduction and oxidation rates suppress Hg^0 production in the upper ocean, weaken seasonal variability, and shift net reduction deeper into the water column. By embedding mercury chemistry into a fully coupled biogeochemical and physical ocean model, POP2/Hg v1.0 offers a process-resolving platform for assessing mercury cycling and its response to environmental change. It enables integrated Earth system simulations and improves predictive capacity for marine mercury under future climate and policy scenarios.

1. Introduction

Hg is a toxic heavy metal with long-range transport potential in the atmosphere. As a persistent pollutant, it can migrate and cycle through the atmosphere, ocean, soil, sea ice, and biota, undergoing complex environmental transformations. Among

https://doi.org/10.5194/egusphere-2025-3880
Preprint. Discussion started: 15 December 2025

these reservoirs, the ocean contains over 50 times the Hg of the atmosphere (Mason et al., 1994), acting as both a major sink and a re-emission source, and therefore plays a central role in the global mercury cycle. The formation of MeHg, one of the most toxic organic mercury compounds, poses a critical risk to global human health. It is estimated that the marine food web is the primary pathway for MeHg bioaccumulation, leading to approximately 9.23–10.07 million IQ point losses globally and 29,000-61,800 fatal heart attacks per year (Zhang et al., 2021; Chen et al., 2025). Therefore, understanding mercury cycling in the ocean is of great significance.

The most important source of mercury to the global ocean is the atmosphere, where the gaseous Hg^0 is oxidized via homogeneous or heterogeneous reactions to Hg^{II} that is subsequently deposited into the ocean through dry and wet deposition processes. Riverine input is one of the sources of mercury to the ocean. Mercury originating from land erosion and wastewater discharge is transported via rivers into marine environments. In addition, sediment release and hydrothermal vents also contribute to oceanic mercury inputs. Within the ocean, a portion of Hg^{II} binds to suspended organic-rich particles, sinking under gravity and delivering mercury to the deep ocean. Another portion undergoes microbial methylation to form MeHg, part of which is taken up by marine plankton, entering the food web, and bioaccumulates in higher trophic-level organisms. Upon death, these organisms release Hg either back into the water column or into sediments. In deep, oxygen-deficient waters, mercury reacts with sulfide to form insoluble mercury sulfide (HgS), which settles stably in sediments. As such, deep-sea sediments act as a long-term reservoir for mercury, effectively removing it from active cycling.

Numerical models have been developed to simulate the ocean mercury cycling and its associated processes, but they remain relatively underdeveloped. Early efforts relied on box models (e.g., Sunderland and Mason, 2007), which provided global mass balance estimates but lacked spatial resolution and representation of biogeochemical processes. Two-dimensional slab models (Soerensen et al., 2010) introduced limited vertical structure but neglected horizontal transport and ocean circulation. The emergence of three-dimensional models improved spatial realism, but most current implementations still face significant limitations. Some models operate in an offline mode, meaning they do not simulate ocean physics in real time but instead rely on precomputed ocean state data. Additionally, the spatial resolution of many models is fixed, limiting their adaptability to different scales or regions. Furthermore, many ocean mercury models are difficult to couple with other Earth system components. For example, the OFFTRAC model (Zhang et al., 2014a) is one of the earliest global 3-D ocean mercury models. It lacks MeHg or DMHg species and does not include any dynamic marine ecosystem. The MITgcm-Hg model (Zhang et al., 2020) incorporates ecological variables from the Darwin ecosystem model. However, the coupling with the ecosystem model is performed offline, based on monthly climatological outputs, and does not permit dynamic feedback between Hg cycling and the marine ecosystem. The model also does not natively support coupling with atmospheric or land surface components, limiting its integration into fully interactive Earth system frameworks. The MERCY v2.0 model (Bieser et al., 2023) provides detailed online coupling between mercury chemistry and a biogeochemical framework, including a plankton food web and particle transport, but it has focused on semi-enclosed seas such as the North and Baltic Seas. It also does not currently include a dynamic sea-ice module and is not coupled to large-scale ocean–atmosphere systems.

https://doi.org/10.5194/egusphere-2025-3880
Preprint. Discussion started: 15 December 2025

The Community Earth System Model version 2 (CESM2) is one of the most advanced global climate modelling frameworks available and provides a promising platform for fully coupled Earth system simulations. In this study, we develop a new global ocean mercury module (POP2/Hg) within CESM2, which simulates key processes such as air–sea exchange, particle partitioning, redox reactions, methylation and demethylation, and mercury transport via the biological pump process. One major advantage is that POP2 is coupled to the Marine Biogeochemistry Library (MARBL), which enables interactive simulation of ecosystem processes, including particulate organic carbon (POC) production and remineralization. MARBL incorporates an online biological pump with separate soft and hard POC pools and simulates sinking particulate organic matter with ballast parameterizations that reflect mineral dust and biogenic material. This improves the representation of particle density, sinking dynamics, and regional variability in carbon transfer efficiency, yielding more realistic POC fluxes from the surface to the mesopelagic ocean (Long et al., 2021). Furthermore, CESM2 already includes dedicated mercury modules for other components, such as CAM6-Chem/Hg for the atmosphere (Zhang and Zhang, 2022), CLM-Hg for terrestrial processes (Yuan et al., 2023), and MOSART-Hg for riverine transport (Peng et al., 2025). This establishes a strong foundation for future full Earth system modelling of mercury, enabling integrated simulations from atmospheric emissions to land erosion, river delivery, and oceanic biogeochemistry.

2 Model description

2.1 Physical Ocean Tracer Model Description

We use the Parallel Ocean Program version 2 (POP2), the ocean component of CESM2, to simulate the global transport and transformation of Hg under present-day conditions. Tracer advection is computed using a third-order upwind-biased scheme, with an optional monotonic flux limiter to minimize numerical dispersion and ensure non-negative concentrations. Vertical mixing is represented using the K-profile parameterization (KPP) scheme, which computes vertical diffusivity and viscosity in the surface boundary layer based on local shear, stratification, and wind forcing. The model is configured on a tripolar curvilinear B-grid, with the North Pole displaced over Greenland to avoid coordinate singularities. It employs 60 vertical z-levels, with enhanced resolution in the upper ocean (~10 m layer thickness) to resolve the mixed layer and thermocline structure. Layer thickness increases with depth to approximately 250 m in the abyss, allowing realistic simulation of both upper-ocean processes and deep-ocean tracer transport (Smith et al., 2010). POP2 has previously been used to simulate inert ocean tracers such as CFC-11, CFC-12, and SF_6, which have been widely applied in evaluating large-scale ventilation and circulation patterns (Dutay et al., 2002). Building on this established framework, we extend POP2 to simulate reactive mercury species by incorporating air–sea exchange, redox reactions, and internal oceanic transformations associated with particulate interactions.

For the development of the mercury module, we introduce five passive tracers, Hg^0, Hg^{II}, two forms of MeHg, monomethylmercury (MMHg) and dimethylmercury (DMHg), and particulate-bound mercury (Hg^p) (Fig. 1). We also consider the various processes of its biogeochemical cycle (see Sect. 2.3). For initial development and spin-up, we use the G ‘Compset’

https://doi.org/10.5194/egusphere-2025-3880
Preprint. Discussion started: 15 December 2025

with the T62_g37 grid configuration, which couples an active ocean and sea ice model with prescribed atmosphere and land components. This setup provides a nominal horizontal resolution of approximately 3°. Marine biogeochemistry is enabled through the default MARBL configuration included in CESM2.1.3. All build settings and source files for this configuration are archived in the Zenodo repository associated with this paper.

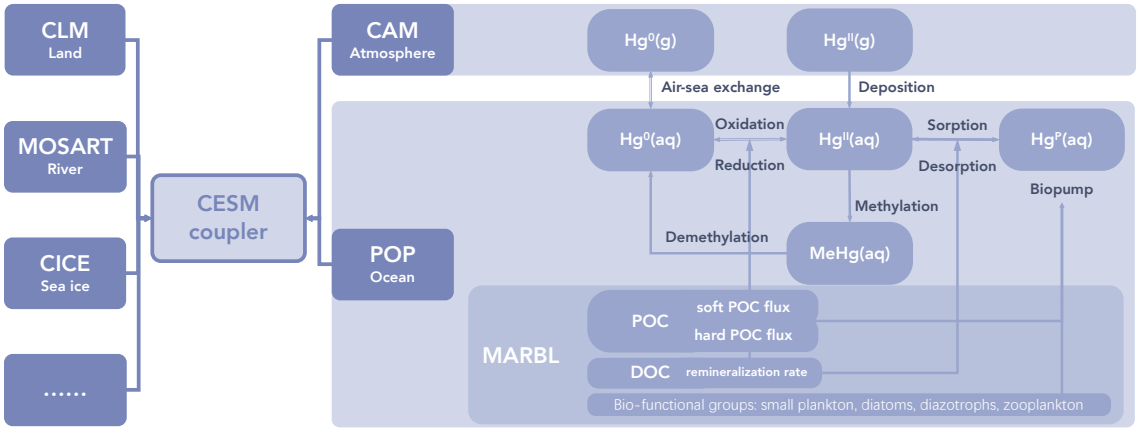

Figure 1: The POP2/Hg v1.0 model framework based on CESM2

2.2 Biogeochemistry: MARBL ecosystem and organic carbon cycling

Marine biogeochemical processes in POP2/Hg v1.0 are simulated using the Marine Biogeochemistry Library (MARBL), a modular component of CESM2 that resolves coupled cycles of carbon, nutrients, plankton ecology, and oxygen dynamics. In the configuration used here, the ecosystem is represented using three phytoplankton functional types, which are small phytoplankton, diatoms, and diazotrophs, and one zooplankton grazer. Each phytoplankton type exhibits distinct physiological traits and nutrient requirements. Small phytoplankton dominate in oligotrophic gyres, diatoms require silicate and are prevalent in upwelling and high-latitude regions, while diazotrophs fix atmospheric nitrogen and are restricted to warm, low-nitrate waters. Zooplankton graze on all three phytoplankton types and recycle nutrients through excretion and respiration. MARBL explicitly simulates cycles of macronutrients (nitrate, phosphate, silicate), iron, oxygen, dissolved inorganic carbon (DIC), alkalinity, and both dissolved and particulate organic matter (DOC, POC). Biogeochemical rates such as photosynthesis, nutrient uptake, remineralization, and particle sinking are computed prognostically at every time step, accounting for ambient light, temperature, nutrient concentrations, and ecological stoichiometry. Remineralization of organic matter releases nutrients and dissolved constituents (e.g., Hg^{II}) back into the water column, strongly modulating vertical tracer profiles (Moore et al., 2001, 2004; Long et al., 2021).

https://doi.org/10.5194/egusphere-2025-3880
Preprint. Discussion started: 15 December 2025

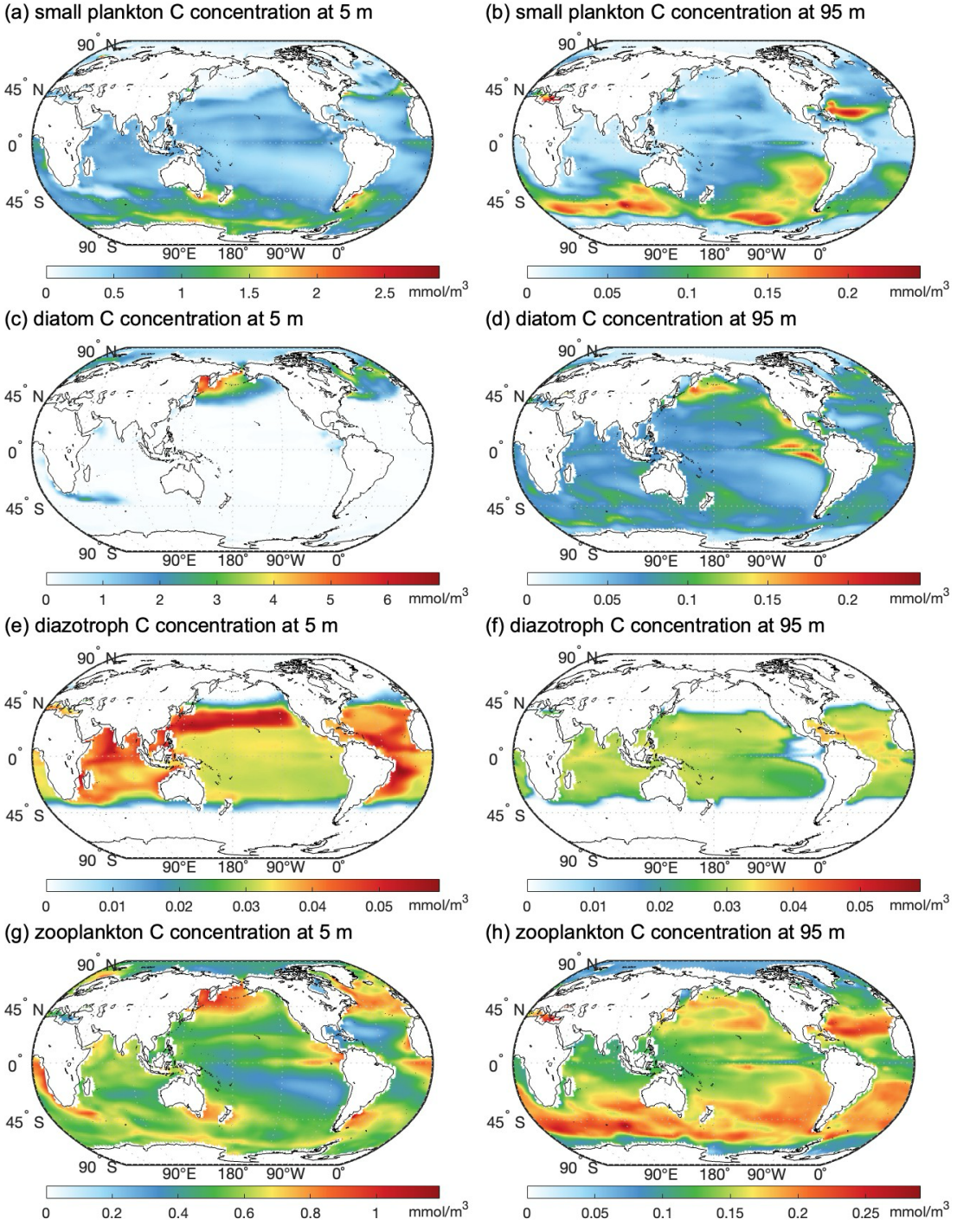

Figure 2: Surface (5 m) and subsurface (95 m) concentrations of biological Carbon simulated by MARBL, units: mmol C.

https://doi.org/10.5194/egusphere-2025-3880
Preprint. Discussion started: 15 December 2025

As shown in Fig. 2, at 5 m depth, the carbon pool of small phytoplankton and zooplankton are widely distributed in low-latitude regions, particularly in oligotrophic gyres and equatorial zones. Diatoms are concentrated in high-latitude areas and eastern boundary upwelling systems (e.g., off Peru and California), reflecting their preference for nutrient-rich conditions. Diazotrophs are abundant in tropical and subtropical regions (Long et al., 2021). At 95 m depth, the concentrations of all biological components decline significantly, consistent with light and nutrient limitation below the euphotic zone. However, POC maintains higher concentrations at 95 m in coastal upwelling zones, indicating active export of organic material and a strong biological pump (Long et al., 2021).

Organic carbon is partitioned into a "soft" POC pool—composed of rapidly sinking detritus that remineralizes over a few hundred meters—and a "hard" or ballasted POC pool with much longer remineralization length scales (~40,000 m), allowing for deep ocean export. These two POC classes are critical for linking ecological production to elemental cycling and are used in our model to drive particle-associated mercury transport (see Sect. 2.3.4). The total POC flux is highest in regions of elevated primary productivity and intense upwelling, such as the eastern equatorial Pacific, northern Indian Ocean, and Arabian Sea, where values exceed 0.1 mmol C cm^{-2} yr^{-1}.

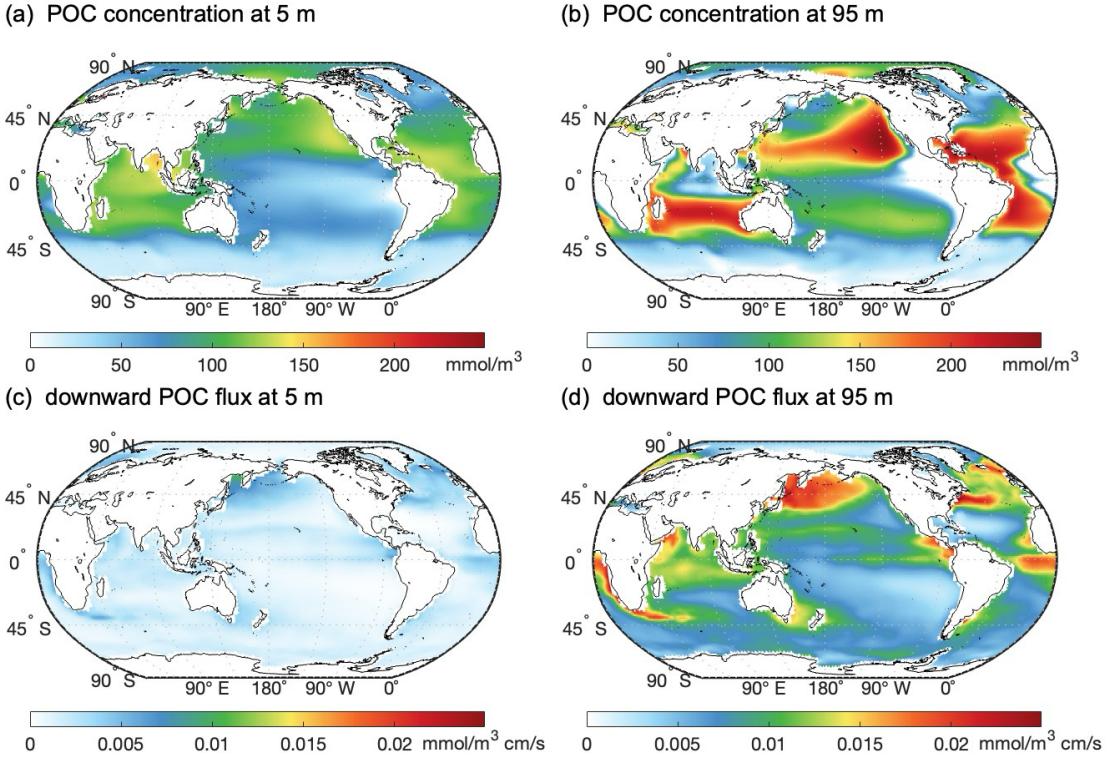

Figure 3: Global maps of total concentration of POC in the ocean (units: mmol m-3): (a) 5 m; (b) 95 m, and total downward POC flux (units: mmol m-3 cm s-1): at (c) 5 m, (d) 95 m

https://doi.org/10.5194/egusphere-2025-3880
Preprint. Discussion started: 15 December 2025

Below 2000 m, the behaviors of soft and hard POC diverge markedly. Soft POC flux becomes nearly negligible across the global ocean at 2889 m (Fig. 4a), due to rapid remineralization in the upper mesopelagic. In contrast, hard POC retains fluxes even at 2889 m (Fig. 4b) and in the deepest layer (Fig. 4d). At the sea floor, hard POC becomes the main source of total POC accumulation (up to 99.96% maximum and an average of 79.21% in fraction).

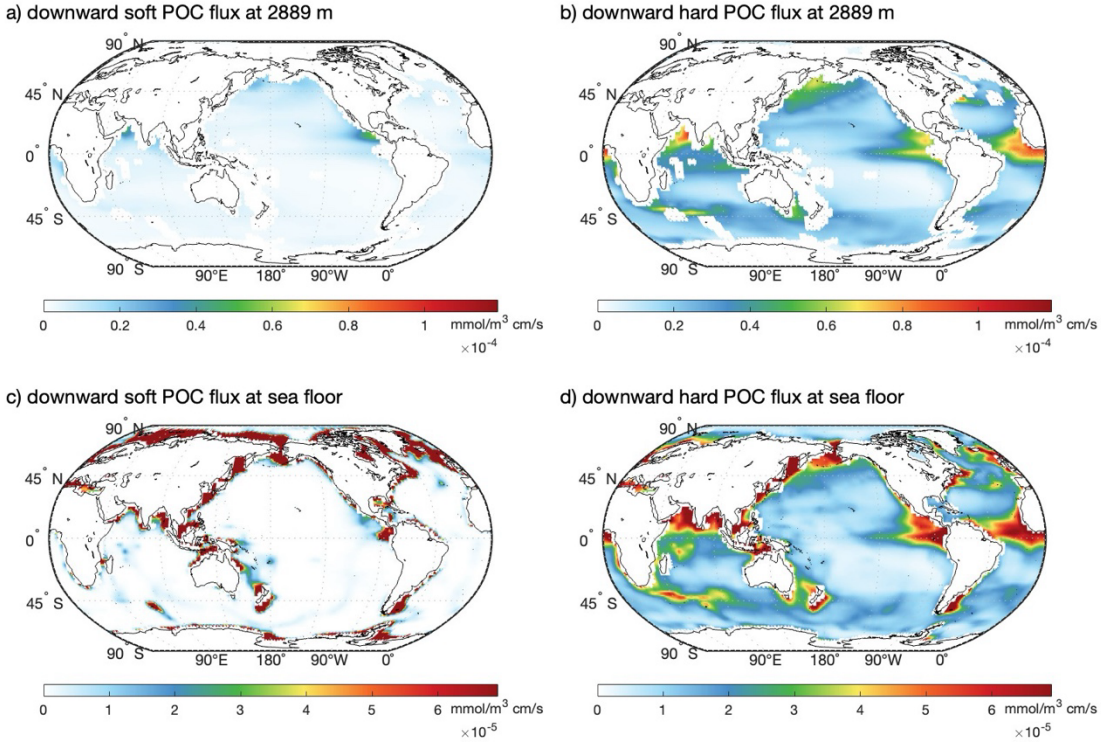

Figure 4: Depth-separated downward flux of soft and hard POC at (a) and (b) 2889 m, and (c) and (d) the deepest layer of the sea, respectively.

The vertical distribution of the organic carbon remineralization rate shows distinct patterns (Fig. 5). At the surface (5 m), Fremin is generally low, as organic matter production exceeds immediate degradation. At 95 m, remineralization peaks in the North Pacific, North Atlantic, Arabian Sea, and eastern equatorial Pacific, coinciding with high POC export. These zones represent areas of high productivity and efficient particle flux attenuation. In contrast, Fremin values in the deeper zone are nearly zero, indicating that most organic matter is remineralized in the upper 200–300 m.

https://doi.org/10.5194/egusphere-2025-3880
Preprint. Discussion started: 15 December 2025

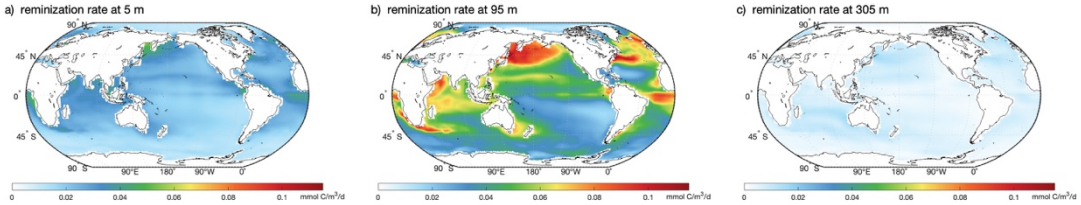

Figure 5: Vertical distribution of organic carbon remineralization flux (Fremin) at (a) 5 m, (b) 95 m, and (c) 305m. Units: mmol C m⁻³ d⁻¹.

2.3 Hg Biogeochemistry in the Ocean

2.3.1 Mercury Chemical Reactions

The primary chemical reactions of mercury species included in the model are listed in Table 1. These reactions include photochemical and biogeochemical processes of Hg^0, Hg^{II}, MMHg and DMHg. Reaction mechanism and kinetic parameters from Zhang et al., (2020) comprise a combination of light-driven and biologically mediated conversions. Methylation converts inorganic mercury (mostly Hg^{II}) to the biologically toxic and bio-accumulative form of MMHg and is a key process in the marine Hg cycle. Demethylation, both photochemical and microbial, serves as a counterbalance by converting MMHg back to Hg^0 or Hg^{II}, modulating its concentration and ecological risk. The methylation-demethylation dynamics are tightly coupled to the marine carbon cycle and microbial remineralization pathways.

Table 1: Kinetic Parameters for Mercury Transformation Reactions in the POP2/Hg v1.0 Model

	reactions	Reaction rate constant parameters
1	$Hg^0 + hv \rightarrow Hg^{II}$	$4.7 \times 10^{-6} \times hv$
2	$Hg^0 \rightarrow Hg^{II}$	$1.3 \times 10^{-9} \times hv + 1.4 \times 10^{-8}$
3	$Hg^{II} + hv \rightarrow Hg^0$	$1.6 \times 10^{-6} \times hv$
4	$Hg^{II} \rightarrow Hg^0$	$2.5 \times 10^{-6} \times OCRR$
5	$Hg^0 \rightarrow Hg^{II}$	$9.9 \times 10^{-6} \times OCRR$
6	$Hg^{II} \rightarrow MMHg$	$4.4 \times 10^{-7} \times OCRR$
7	$MMHg \rightarrow Hg^0$	$1.1 \times 10^{-8} \times exp\left(5457 \times \frac{1}{T_c} - \frac{1}{T_k}\right)$

https://doi.org/10.5194/egusphere-2025-3880
Preprint. Discussion started: 15 December 2025

8	$MMHg + hv \rightarrow Hg^{II}$	8.0×10^{-8}
9	$MMHg \rightarrow DMHg$	9.3×10^{-9}
10	$DMHg + hv \rightarrow MMHg$	$3.8 \times 10^{-9} \times hv + 1.9 \times 10^{-8}$

2.3.2 Air–Sea Gas Exchange of Hg^0 and DMHg

The ocean-atmosphere exchange of Hg^0 and DMHg is modelled based on the concentration gradient across the air-sea interface, modulated by solubility (Henry's law constant), the Schmidt number, and sea ice coverage. The net flux direction—either evasion or deposition—is governed by the surface saturation ratio of dissolved Hg species relative to atmospheric concentrations.

The gas transfer velocity PV, also referred to as the piston velocity, is derived from the reference CO_2 transfer velocity and corrected for the sea-ice fraction and the Schmidt number of the target species:

$$PV = (1 - f_{ice}) \cdot PV_{CO_2} \cdot \sqrt{\frac{Sc_{CO_2}}{Sc_{Hg}}} \quad (1)$$

where f_{ice} is the fraction of sea ice, and Sc_{Hg} and Sc_{CO_2} are the Schmidt numbers of the target mercury species and CO_2, respectively. The Schmidt numbers for Hg^0 and DMHg are calculated following Soerensen et al., (2010) and (Black et al., 2009), accounting for dependencies on sea surface temperature (SST) and salinity (SSS):

$$Sc_{Hg0} = \frac{\nu}{D_{Hg0}}, Sc_{DMHg} = \frac{\nu}{D_{DMHg}} \quad (2)$$

where ν is the kinematic viscosity of seawater, and D is the diffusivity.

With the gas transfer velocity defined, the net air–sea exchange flux F for each gaseous mercury species is then calculated as:

$$F = PV \cdot (C_{sat} - C_{surf}) \quad (3)$$

where PV is the gas transfer velocity (corrected for Schmidt number), C_{surf} is the surface concentration, and C_{sat} is the equilibrium concentration determined by Henry's law:

$$C_{sat} = \frac{C_{air}}{H} \quad (4)$$

https://doi.org/10.5194/egusphere-2025-3880
Preprint. Discussion started: 15 December 2025

2.3.3 Sorption of Hg^{II} onto particles

The reversible partitioning of Hg^{II} onto suspended particles is an important process controlling the geochemical species, transport, and bioavailability of the element in the ocean. Organic-rich particles, such as detritus, biogenic material (e.g., plankton), or mineral clays, are also able to bind Hg^{II}. This particulate-bound mercury (Hg^{P}) can then undergo gravitational settling, promoting the vertical transport and potential removal from the surface ocean. Hg^{P} is subject to gravitational settling, facilitating vertical transport and potential removal from the surface ocean. In the model, we represent this process through an instantaneous equilibrium partitioning between dissolved Hg^{II} and particulate-bound Hg^{P}, following a linear partitioning assumption (Morel et al., 1998):

$$\frac{Hg^{p}}{Hg^{II}{}_{aq}} = \frac{k_d}{f_{oc}}[POC] \quad (5)$$

where k_d is the partition coefficient and f_{oc} is the organic carbon fraction of suspended particles (assumed to be 10% following Strode et al., 2010), and $[POC]$ is the modelled particulate organic carbon concentration from MARBL. Unlike prior studies that applied climatological surface POC fields (e.g., Zhang et al., 2014a), we dynamically calculate this partitioning using the vertically resolved and time-evolving POC fields from MARBL.

2.3.4 Biological Pump Transport of Particulate Hg

Hg^{P} is simulated in our model by coupling it to the vertical transport of POC as diagnosed by the MARBL ecosystem module. MARBL resolves two classes of POC with distinct biogeochemical behaviors: soft POC, which is labile and sinks rapidly but is typically remineralized within the upper hundreds of meters; and hard POC, which is associated with ballasted particles and exhibits slow degradation over length scales up to ~40,000 m, enabling long-distance transport into the deep ocean.

We assume that inorganic Hg^{II} partitions onto organic particles via a fixed distribution coefficient (see section 2.2), and that once adsorbed, the resulting Hg^{P} is vertically exported alongside the particles. The effective sinking rate of Hg^{P} is dynamically computed using the ratio of total particulate flux to total particulate concentration:

$$v_{sink\_soft} = \frac{F_{POC\_soft} + F_{bioC}}{POC_{soft} + bioC} \quad (6)$$

$$v_{sink\_hard} = \frac{F_{POC\_hard} + F_{bioC}}{POC_{hard} + bioC} \quad (7)$$

Here, $F_{POC_{out}}$ represents the sinking flux of non-living detrital POC, while $F_{bioC\,out}$ represents the flux associated with phytoplankton biomass (e.g., small phytoplankton, diatoms, and diazotrophs). The denominator includes the in-situ concentrations of POC and living particulate biomass (bioC).

The vertical flux of Hg^{P} is then given by:

$$f_{out\_soft} = v_{sink\_soft} \cdot Hgp \quad (8)$$

https://doi.org/10.5194/egusphere-2025-3880
Preprint. Discussion started: 15 December 2025

$$f_{out\_hard} = v_{sink\_hard} \cdot Hgp \quad (9)$$

A maximum velocity of 0.5 m d^{-1} is imposed to guarantee physical consistency and to prevent excessive export in oligotrophic regimes.

This formulation allows the sinking rate of Hg^p to vary dynamically in space and time, responding to ecological processes such as phytoplankton blooms, detritus production, and aggregation. As particles sink and undergo remineralization or grazing, the associated Hg^p is removed from the water column, either lost to sedimentation or recycled via desorption and re-equilibration with the dissolved phase. At the seafloor, Hg^p is assumed to be deposited, with partial burial and possible benthic recycling.

2.4 Atmospheric Deposition Input and Observation Dataset

The model uses two forms of atmospheric mercury input: atmospheric Hg^0 concentration and Hg^{II} deposition (Fig. 6). Surface forcing fields for Hg^0 and Hg^{II} mercury are prescribed from the CAM6-Chem/Hg model. Hg^0 forcing is strongest in the western Pacific, matching anthropogenic source distributions. Hg^{II} deposition dominates in the intertropical convergence zone (ITCZ), North Indian Ocean, and eastern equatorial Pacific—consistent with wet deposition patterns driven by deep convection. Atmospheric Hg^0 concentration is prescribed from CAM6-Chem/Hg output (Zhang and Zhang, 2022), allowing for both climatological and interannually varying forcing scenarios. Previous studies (Zhang et al., 2015) suggested that riverine Hg has limited impacts on the open ocean, so the current model does not yet include riverine mercury input and focuses on the development and evaluation of the ocean module, where atmospheric inputs are sufficient. The coupling with riverine inputs and the land component will be incorporated in future work.

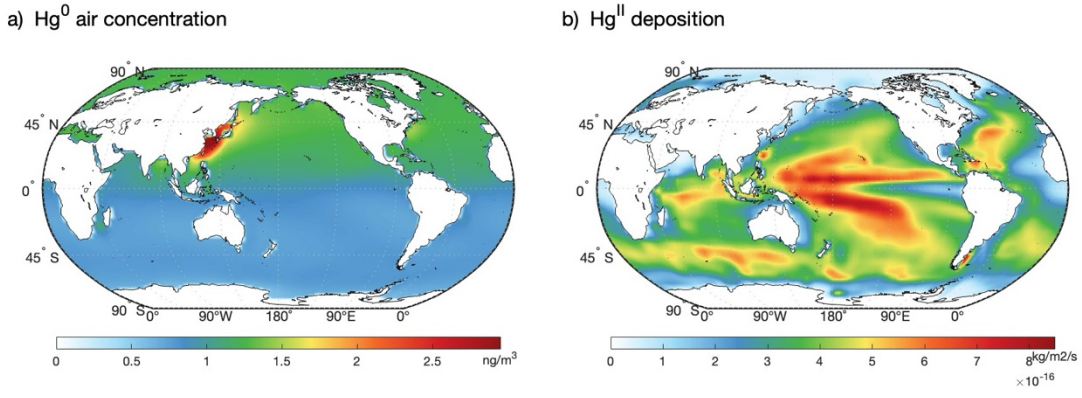

Figure 6: Atmospheric mercury input fields used as model forcing: (a) atmospheric Hg^0 concentration, units: ng m^{-2} d^{-1} and (b) Hg^{II} deposition, units: mol m^{-2} s^{-1}.

The model evaluation utilized a compiled dataset of surface ocean Hg^0 concentrations provided by Zhang et al. (2020), and air-sea exchange flux collected by Kuss et al., (2011), Soerensen et al., (2014, 2013), Wang et al., (2017), Kalinchuk et al.,

https://doi.org/10.5194/egusphere-2025-3880
Preprint. Discussion started: 15 December 2025

(2021), and Nerentorp Mastromonaco et al., (2017). These data were used to validate model outputs and to calibrate the air–sea exchange parameterizations.

3. Results

3.1 Hg^0

The modelled dissolved elemental mercury (Hg^0) concentrations in surface waters range from 10 to 120 fM, accounting for approximately 10 % of Hg^T in the upper ocean (Fig. 7a). High concentrations (> 80 fM) are modelled in the western Pacific warm pool, equatorial western Atlantic, North Indian Ocean, and Caribbean Sea. In contrast, the Southern Ocean and eastern equatorial Pacific show notably low Hg^0 levels (< 30 fM). These patterns are driven by sea surface temperature, solar irradiance, and wind speed: warmer, low-latitude regions with high light availability and low wind speeds favor photoreduction of Hg^{II} and reduced evasion, allowing accumulation of Hg^0 in surface waters.

Fig. 7a) presents the spatial distribution of modelled surface Hg^0 along with pointwise observations for comparison. The model reproduces elevated Hg^0 concentrations in tropical and subtropical regions reasonably well, particularly in the western Pacific, Indian Ocean, and South Atlantic, ranging from 0.04 pM to 0.08 pM. However, significant discrepancies occur in coastal and estuarine zones such as Southeast Asia and the eastern seaboard of North America, where observed values frequently exceed 0.2 pM, while simulated Hg^0remain around 0.07 pM. These differences likely result from the lack of riverine Hg input, sea ice melting, and limited resolution nearshore, which are not yet incorporated in the model. Overall, the simulated large-scale gradients are consistent with known biogeochemical and physical drivers.

https://doi.org/10.5194/egusphere-2025-3880
Preprint. Discussion started: 15 December 2025

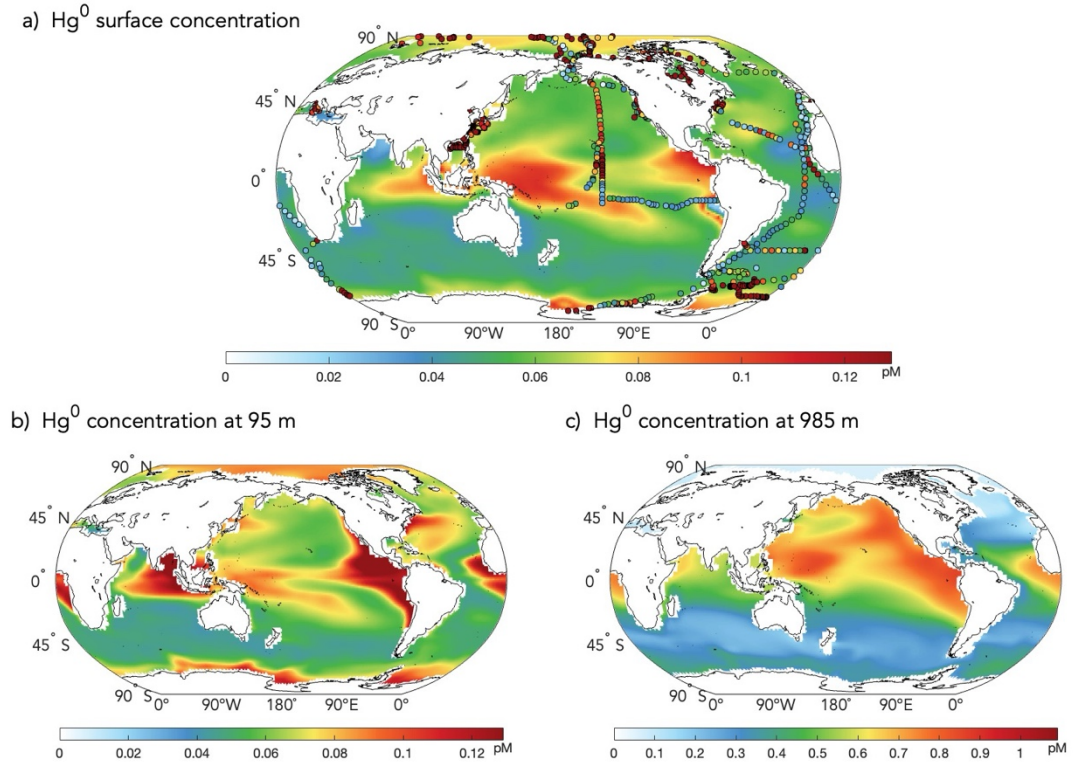

Figure 7: Modelled Hg^0 concentrations in the ocean (units: pM): (a) surface (5 m) concentrations with scattered observations; (b) 95 m depth; (c) 985 m depth.

255

At 95 m depth, the modelled Hg^0 concentrations typically range from 0.02 to 0.08 pM and in some regions slightly exceed surface values. This increase is particularly evident in upwelling and remineralization zones such as the eastern equatorial Pacific, Arabian Sea, and the subtropical boundary currents. At this depth, light attenuation limits photoreduction, while remineralization-driven Hg^{II} reduction increases the fraction of Hg^0, combined with weaker air–sea exchange rates that allow
260 greater retention of Hg^0. In the deep ocean (around 1000 m), Hg is transported via the downward sinking of Hg^P, followed by remineralization and release as dissolved Hg^{II} within the 500–1000 m depth range (Zhang et al., 2014b). Hg^{II} can then be converted to Hg^0 through microbially mediated or non-photochemical redox reactions, leading to elevated Hg^0 concentrations at depth (Zhang et al., 2020). In addition, the initial condition of the model features relatively high deep-ocean Hg^0 concentrations, which contribute to a pronounced increase in simulated Hg^0 levels at 1000 m (up to 0.8 pM) compared to
265 shallower depths.

https://doi.org/10.5194/egusphere-2025-3880
Preprint. Discussion started: 15 December 2025

3.2 Hg^{II}

The simulated distribution of Hg^{II} reflects the combined influence of atmospheric deposition, redox transformations, and internal cycling. At the sea surface (Fig. 8a), Hg^{II} concentrations range from approximately 0.1 to 0.8 pM, with elevated values in the North Indian Ocean, tropical western Pacific, and parts of the South China Sea. These regions coincide with intense wet and dry deposition of atmospheric Hg^{2+} and zones of active photochemical cycling. Extreme values occur in biologically productive or upwelling regions, such as the Bay of Bengal and Southeast Asian marginal seas, where concentrations reach up to 1.8 pM.

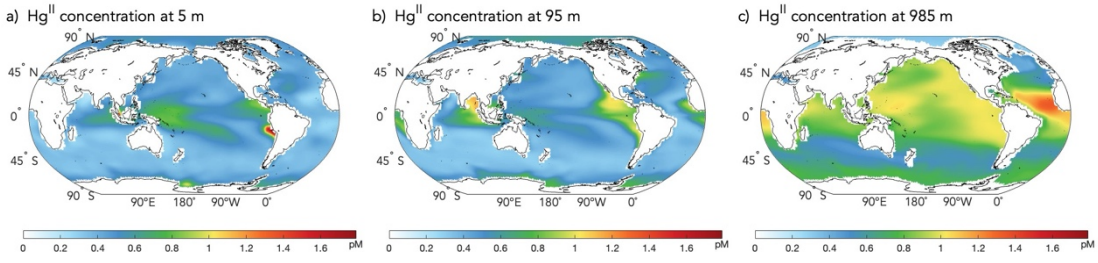

Figure 8: Modelled concentration of Hg^{II} in the ocean (units: pM): (a) surface (~5 m); (b) 95 m; (c) 985 m.

At 95 m depth (Fig. 8b), Hg^{II} concentrations are markedly enhanced in high-productivity or upwelling regions, including the eastern equatorial Pacific and the Arabian Sea, typically ranging from 0.5 to 1.2 pM. This enhancement is primarily due to the downward export and remineralization of Hg^{p}, combined with reduced photoreduction efficiency that limits the conversion to Hg^{0}. In addition, oxygen-deficient zones at this depth promote the persistence of divalent mercury, making them key sources of microbial methylation. In the deep ocean (~985 m, Fig. 8c), Hg^{II} becomes the dominant dissolved mercury species. High concentrations are observed in the North Pacific and equatorial Atlantic, approaching 1.5 pM.

The simulated Hg^{p} reflects the combined influences of particulate POC and Hg^{II} in both horizontal and vertical dimensions. At the ocean surface (Fig. 9a), Hg^{p} concentrations exhibit distinct regional maxima in the northwestern Indian Ocean, equatorial Atlantic, and northeastern Pacific, particularly in the Bay of Bengal and Gulf of Mexico, where values exceed 0.3 pM. elevated Hgp concentrations are co-located with regions where both POC levels and HgII concentrations are relatively high (see Figs. 8a and 10a), promoting enhanced sorption of HgII onto organic particles.

https://doi.org/10.5194/egusphere-2025-3880
Preprint. Discussion started: 15 December 2025

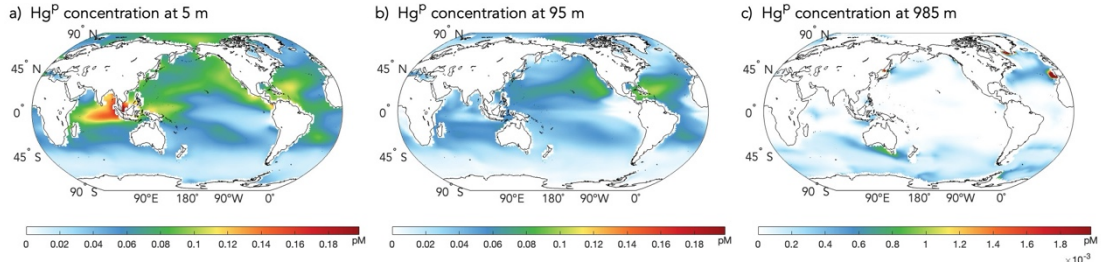

Figure 9: Modelled concentration of Hg^p in the ocean (units: pM): (a) surface 5 m; (b) 95 m; (c) 985 m.

At 95 m depth (Fig. 9b), Hg^p concentrations get lower, with the highest values (up to 0.07 pM) persisting in subsurface convergence and export regions such as the western Pacific and eastern equatorial Atlantic. The influence of POC dominates over that of Hg^{II}, as high Hgp concentrations closely correspond to regions of elevated POC. In deep sea (around 1000 m), where biological productivity declines sharply (< 0.02 pM), Hg^p concentrations nearly vanish. At this depth, the dominant process becomes remineralization, and nearly all Hg^p is converted back to the dissolved form, with notable residual Hg^p concentrations only persisting in localized regions where POC remains. This vertical attenuation of Hg^p aligns with previous modeling and observational studies (e.g., Sunderland and Mason, 2007; Zhang et al., 2014b).

3.3 MeHg

The simulated distribution of MeHg, including MMHg and DMHg, exhibits pronounced vertical and regional gradients shaped by subsurface methylation, biological productivity, and redox conditions. At the surface (Fig. 10a), MeHg concentrations remain generally low across most of the global ocean, typically below 0.05 pM. However, due to strong photo-demethylation and rapid air–sea exchange of volatile DMHg, surface MeHg remains significantly depleted relative to deeper layers. This indicates that surface MeHg is tightly regulated by photochemical loss and air–sea fluxes (Soerensen et al., 2010; Zhang et al., 2020). These surface patterns correspond reasonably well with available observations, particularly in the North Pacific and northeastern Atlantic, where both modelled and observed values are within the range of 0.02–0.10 pM.

https://doi.org/10.5194/egusphere-2025-3880
Preprint. Discussion started: 15 December 2025

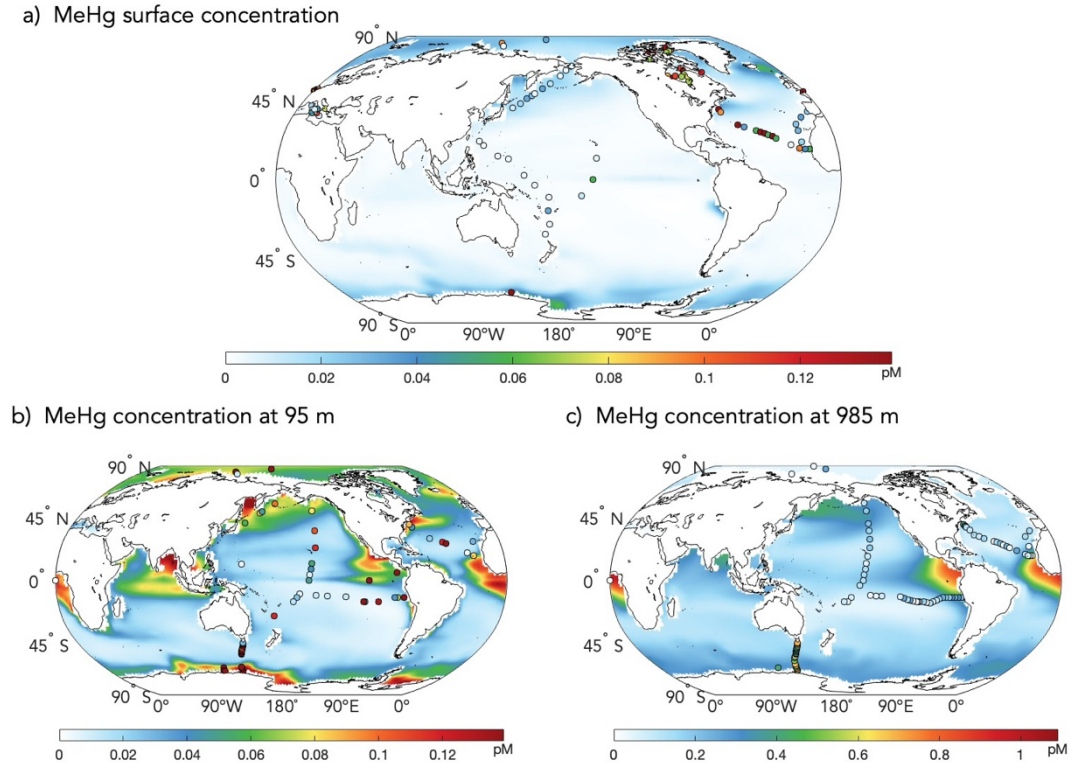

305 **Figure 10: Modelled concentration of MeHg compared with observation in the ocean (units: pM): (a) surface (~5 m); (b) 95 m; (c) 985 m.**

At 95 m depth (Fig. 10b), peak MeHg concentrations occur in regions of high productivity or upwelling, such as the eastern tropical Pacific, the Arabian Sea, and the northern Indian Ocean, with simulated values reaching up to ~0.12 pM. closely
310 matching observed hotspots along the eastern boundary currents (e.g., Peru and California coasts). The agreement with observations is particularly strong in the North Pacific and tropical Atlantic, where observed MeHg concentrations fall within 0.04–0.12 pM, similar to modelled values.

In the deep ocean (985 m, Fig. 10c), the model simulates widespread accumulation of MeHg, with background values around 0.1–0.3 pM, and local maxima exceeding 0.6–0.8 pM in the North Pacific interior. These elevated values are consistent with
315 observations from deep sampling campaigns, especially in the North Pacific Subarctic Gyre and Equatorial Pacific, where deep MeHg concentrations often exceed 0.5 pM. The persistence of MeHg at these depths is likely sustained by slow degradation rates and limited transport, allowing accumulation over longer timescales. This pattern is consistent with previous global ocean mercury models (e.g., Zhang et al., 2014b; Wang et al., 2023).

https://doi.org/10.5194/egusphere-2025-3880
Preprint. Discussion started: 15 December 2025

However, notable discrepancies remain. In the Southern Ocean and certain subtropical gyres, the model tends to underestimate MeHg concentrations, with values often below 0.009o4 pM, while observations in these regions suggest higher levels (up to 0.13 pM). This mismatch may arise from unresolved fine-scale remineralization processes or microbial methylation in oxygen minimum zones that are not well captured at the model's spatial resolution.

3.4 Hg^T

At the surface (Fig. 11a), simulated Hg^T concentrations range from 0.1 to 2.0 pM, with higher values (>1.2 pM) found in the eastern equatorial Pacific, western boundary currents (e.g., Gulf Stream, Kuroshio), and eastern boundary upwelling zones (e.g., off Peru and southwest Africa). The patterns agree reasonably well with observational data (dots in Fig. 11a) in open ocean settings, especially in the Pacific and Indian Oceans, where simulated Hg^T falls within the observed range (typically 0.5–1.2 pM), especially in regions with strong atmospheric deposition or coastal influence. For example, in the North Atlantic Ocean (excluding coastal regions), observed THg concentrations at the surface range from 0.6 ± 0.2 pM, while the model simulates values around 0.7 ± 0.1 pM. In contrast, the model underestimates Hg^T in some coastal and marginal seas, including Southeast Asia, the Gulf of Mexico, and the western North Atlantic shelf. These mismatches likely arise from the exclusion of riverine Hg inputs and insufficient resolution of shelf and margin dynamics in the current model configuration.

https://doi.org/10.5194/egusphere-2025-3880
Preprint. Discussion started: 15 December 2025

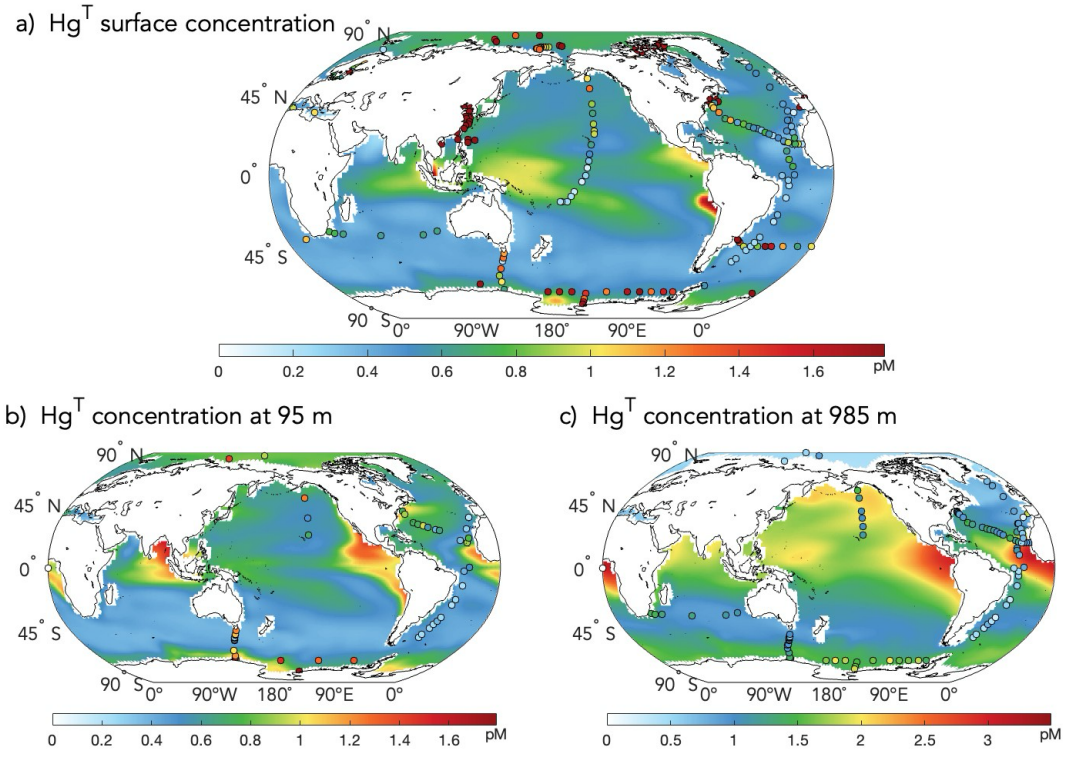

Figure 11: Modelled Hg^T concentration compared with observation: (a) at 5 m and (b) at 95 m in year 10 (balanced state). Units: pM.

At 95 m depth (Fig. 11b), elevated concentrations persist in eastern boundary regions and extend westward into the tropical Atlantic and Pacific basins. Simulated Hg^T values typically range from 0.4 to 1.4 pM at this depth, showing good agreement with observation.

In deeper waters (985 m, Fig. 11c), Hg^T shows widespread accumulation, especially in the North Pacific, equatorial Atlantic, and Southern Ocean, where values exceed 2.0 pM in several regions. This pattern reflects the integrated effect of particle-bound Hg transport and deep remineralization. In the North Pacific, deep-ocean concentrations (985 m) observed at 2.1 ± 0.3 pM are closely matched by simulated values of 2.3 ± 0.2 pM. In parts of the Atlantic Ocean and the Southern Ocean, the model tends to overestimate deep Hg^T relative to observations. A possible contributor is the lack of explicit sediment–water exchange or resuspension mechanisms, which are known to influence mercury dynamics in deep basins, especially in marginal seas and slope regions. Without accounting for benthic fluxes, the model may compensate by accumulating Hg in the water column.

https://doi.org/10.5194/egusphere-2025-3880
Preprint. Discussion started: 15 December 2025

4. Mercury Transformation and Vertical Fluxes

4.1 Air–Sea Exchange

The ocean surface acts as the primary interface for the exchange of Hg^0 between the atmosphere and the ocean. Model simulations estimate a global net evasion flux of Hg^0 to the atmosphere at approximately 4.43 Mg yr^{-1}, consistent with previous studies. Atmospheric deposition of Hg^{II} is estimated at 4.20×10^3 t yr^{-1}, suggesting a near-equilibrium exchange. Additionally, DMHg contributes a net evasion of 67.48 t yr^{-1}.

Spatially, Hg^0 evasion is strongest in tropical and subtropical regions, where warm surface waters and high solar radiation enhance photoreduction and lead to Hg^0 supersaturation. Elevated fluxes are also observed in the South Pacific and Indian Ocean. Along the western boundary of the North Atlantic, enhanced evasion is driven by the Gulf Stream's elevated temperatures and wind speeds. The Southern Ocean shows strong evasion as well, attributed to persistent westerlies and high wind forcing.

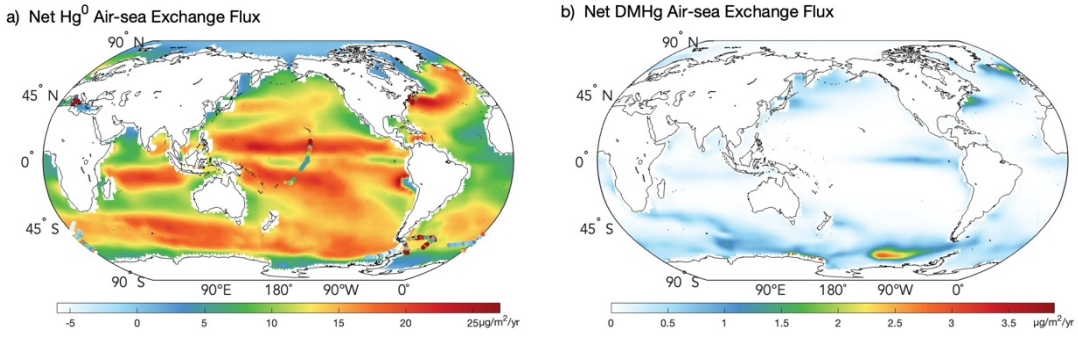

Figure 12: Air-sea exchange flux of Hg^0 (with observations) and DMHg.

4.2 Chemical Transformation

Inorganic mercury transformations in the ocean, including redox and methylation reactions, vary with depth, region, and season (Fig. 13–15). At the surface (0–50 m), photoreduction of Hg^{II} dominates, especially in low-latitude regions. The annual integrated flux of Hg^{II} reduction reaches 1.53×10^5 t yr^{-1}, with maxima in the equatorial Pacific, North Atlantic gyres, and the Indian Ocean (>40 μg m^{-3} yr^{-1}), consistent with intense solar irradiance and shallow mixed layers.

https://doi.org/10.5194/egusphere-2025-3880
Preprint. Discussion started: 15 December 2025

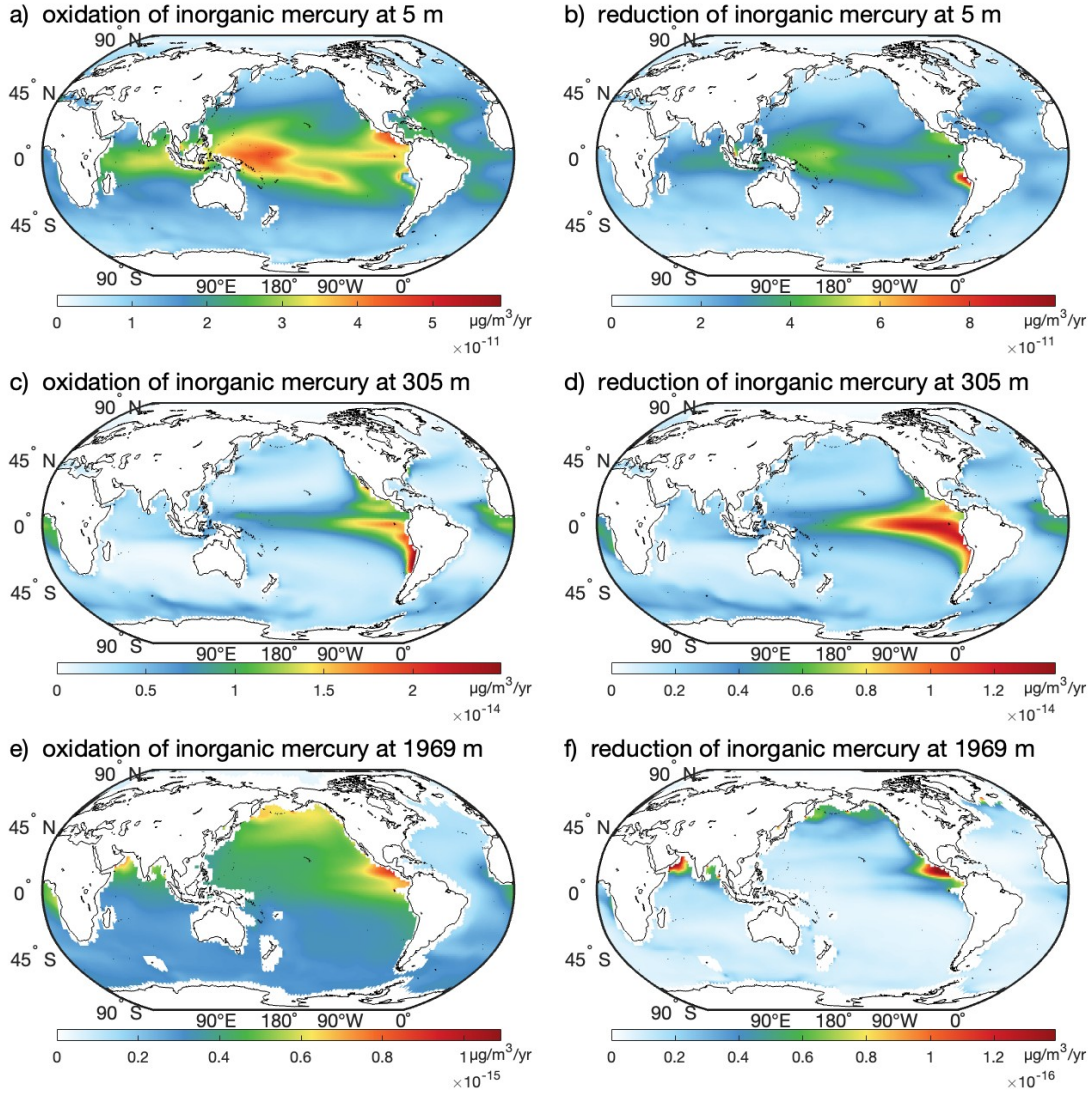

Figure 13: Spatial distribution of inorganic mercury redox transformations at three depths. a), c), e) Oxidation from Hg0 to HgII; b), d), f) Reduction from HgII to Hg0. Panels correspond to depths of 5 m, 305 m, and 1969 m, respectively.

370

At intermediate depths (50–1000 m), net reduction still prevails, with an annual total flux of 1.74×10^2 t yr^{-1}. Both oxidation and reduction rates at 305 m (Fig. 13c-d) are roughly three orders of magnitude lower than surface values, but oxidation becomes dominant in certain mid-depth waters, notably in the North Atlantic and eastern equatorial Pacific upwelling zones. In the deep ocean (under 1000 m, Fig. 13e–f), redox fluxes further diminish (on the order of 10^{-4} μg m^{-2} yr^{-1}), and a net
375 oxidation trend emerges, with a cumulative flux of 3.74×10^3 t yr^{-1}, suggesting slow but sustained chemical transformation of Hg^0 to Hg^{II} in deep waters.

https://doi.org/10.5194/egusphere-2025-3880
Preprint. Discussion started: 15 December 2025

The spatial distributions of methylation and demethylation rates are closely linked to the modelled Hg^{II} concentrations and organic matter remineralization patterns (Fig. 3 and 5). Regions of enhanced methylation tend to coincide with strong remineralization zones, particularly at 95 m depth in the eastern tropical Pacific, the northwest Pacific, and the Arabian Sea. Besides, the regeneration of Hg^{II} from sinking organic matter plays a key role in promoting MeHg production. While in surface waters (5 m depth), demethylation dominates, reflecting efficient photochemical and microbial degradation processes under high light conditions.

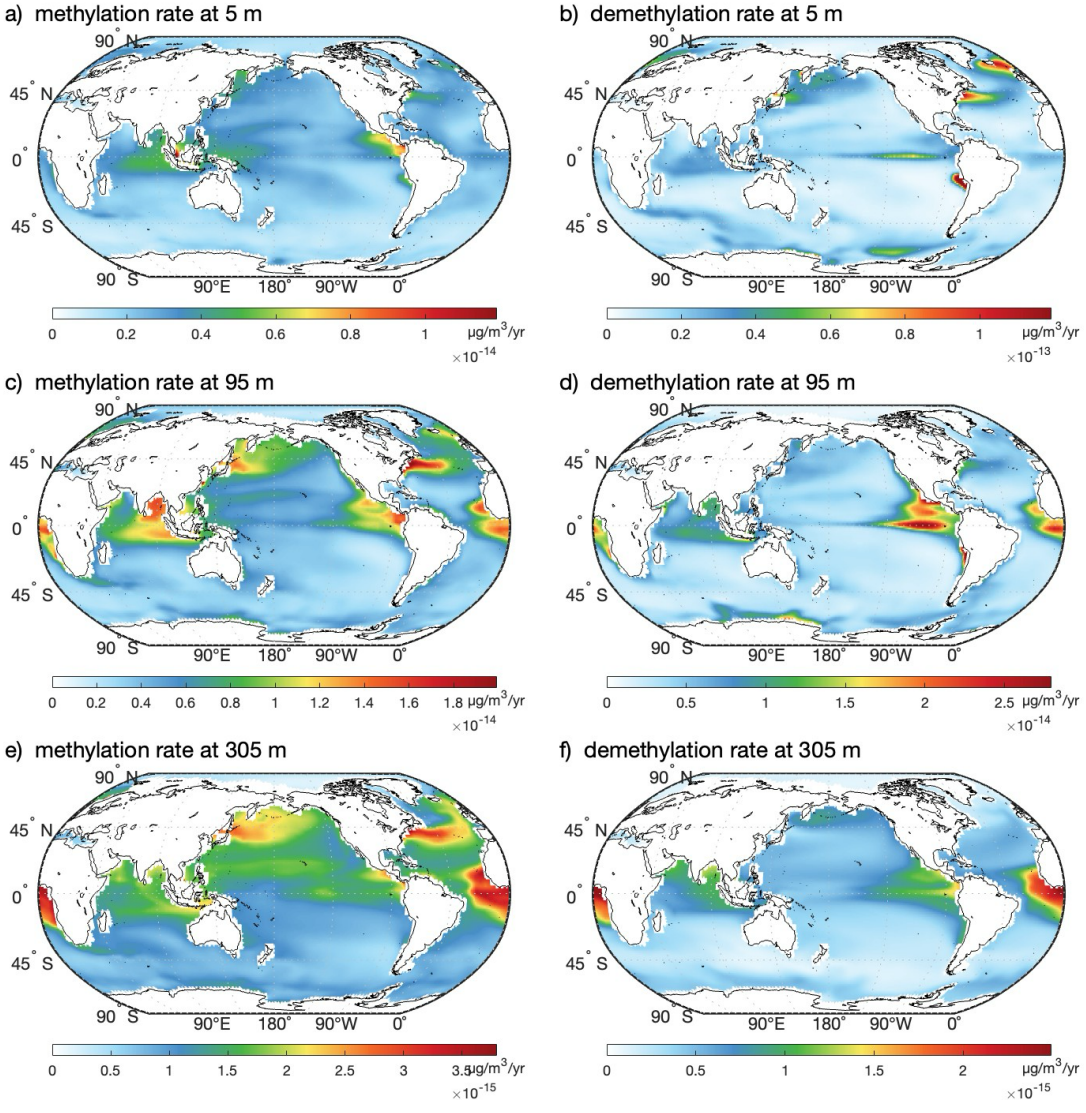

Figure 14: a), c), e) Methylation and b), d), f) demethylation of mercury species across 5 m, 95 m, and 305 m, respectively.

https://doi.org/10.5194/egusphere-2025-3880
Preprint. Discussion started: 15 December 2025

Annual demethylation fluxes reach 1.31×10^3 t yr^{-1} in surface waters, 2.71×10^3 t yr^{-1} in the subsurface, and 3.46×10^3 t yr^{-1} in the deep ocean. Methylation hotspots align with remineralization zones, especially in the eastern tropical Pacific, the northwest Pacific, and the Arabian Sea. These processes are supported by regenerated Hg^{II} from sinking organic matter. However, the relatively coarse horizontal resolution of the model may lead to an underestimation of localized methylation or demethylation hotspots in these regions.

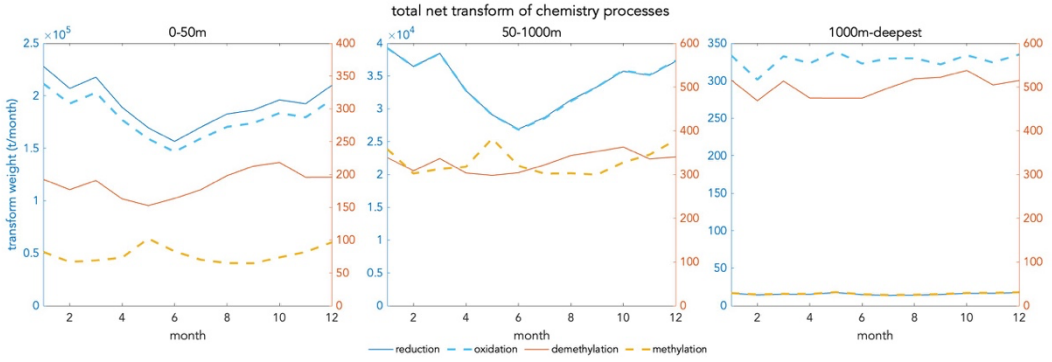

Figure 15: Monthly net transformation fluxes in different ocean depth layers (0–50 m, 50–1000 m, >1000 m).

Seasonal variation is pronounced in surface redox fluxes, with higher rates in spring and summer (Fig. 15). Methylation and demethylation show less seasonality and remain active throughout the year, especially at depths >1000 m, where conditions are more stable.

4.3 Biological Pump and Vertical Transport

As shown in Fig. 16, the downward flux of Hg^p associated with soft and hard POC exhibits distinct spatial and vertical patterns, coinciding with the contribution of soft and hard POC fluxes (Fig. 3 and 4). At 5 m depth, elevated Hg^p fluxes are observed in coastal and upwelling regions, particularly in the eastern equatorial Pacific, the Arabian Sea, and the Peru upwelling system. Soft POC dominates the near-surface Hg^p transport, with maximum fluxes reaching up to 8×10^{-3} fmol cm^{-3} s^{-1}, whereas hard POC contributes much less, typically below 2×10^{-5} fmol cm^{-3} s^{-1} and accounting for only 0.97% of the total. In surface waters (0–50 m), the export of Hg^p on POC proceeds at a rate of 7.08×10^2 t yr^{-1}.

At 95 m depth (Fig. 16c–d), Hg^p fluxes decrease by one to two orders of magnitude, yet soft POC still contributes substantially. Integrated over the upper 1000 m, soft POC is responsible for 98.62% of the total Hg^p flux, while hard POC accounts for only 1.37%, consistent with its lower proportion in total POC fluxes in the upper ocean. Within the midwater column (50–1000 m), remineralization dominates, releasing dissolved Hg species, while Hg^p accumulation peaks at 6.87×10^2 t yr^{-1}, closely aligned with regions of high POC production and microbial activity.

https://doi.org/10.5194/egusphere-2025-3880
Preprint. Discussion started: 15 December 2025

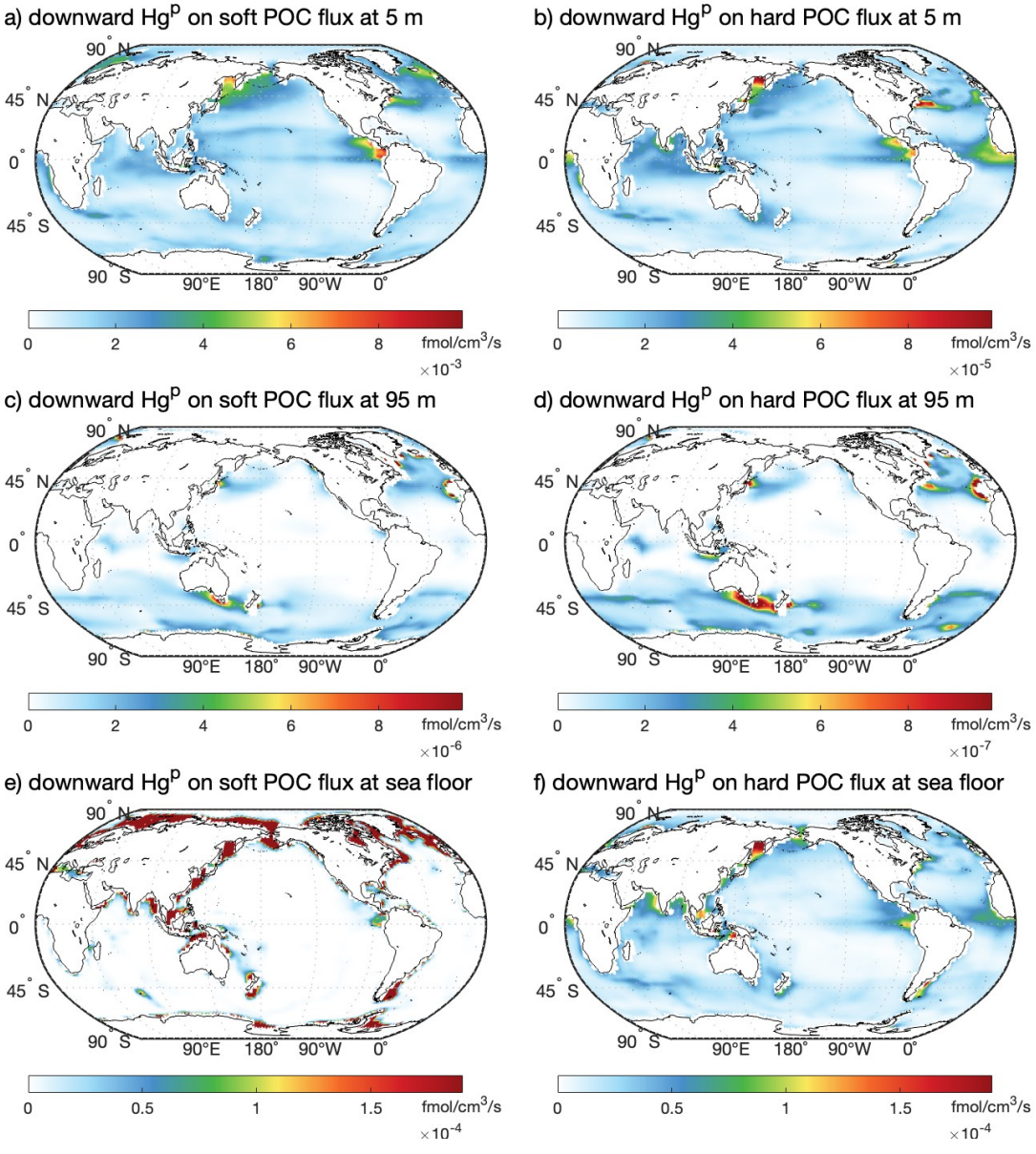

Figure 16: Vertical distribution of Hgp fluxes associated with soft and hard POC at 5 m, 95 m, and the sea floor.

In contrast, the contribution pattern reverses at the seafloor (Fig. 16e–f), although only 0.19 t yr^{-1} of Hg^p reaches the seafloor. Under 1000m, most of the Hg^p has been removed. Hard POC becomes the dominant vector of Hg^p delivery to sediments, particularly in oligotrophic subtropical gyres and deep basins, where it contributes up to 99.96% of the total Hg^p flux. The persistence of hard POC at depth supports its role as the principal carrier of Hgp below 1000 m. However, its impact on deep-

https://doi.org/10.5194/egusphere-2025-3880
Preprint. Discussion started: 15 December 2025

ocean Hg^p inventories remains limited due to both the small Hg load and the continued degradation of POC. Overall, the biological pump redistributes mercury vertically via particle-associated transport, with pronounced stratification.

4.4 Sensitivity to redox chemistry

To assess the model's sensitivity to redox rates, we conducted a 20-year simulation with reduced photochemical reaction rates following (Bieser et al., 2023): the oxidation rate of Hg^0 was lowered from 4.7×10^{-6} s^{-1} to 2.4×10^{-7} s^{-1}, and the reduction rate of Hg^{2+} was decreased from 1.6×10^{-6} s^{-1} to 1.0×10^{-8} s^{-1}, while all other parameters remained unchanged.

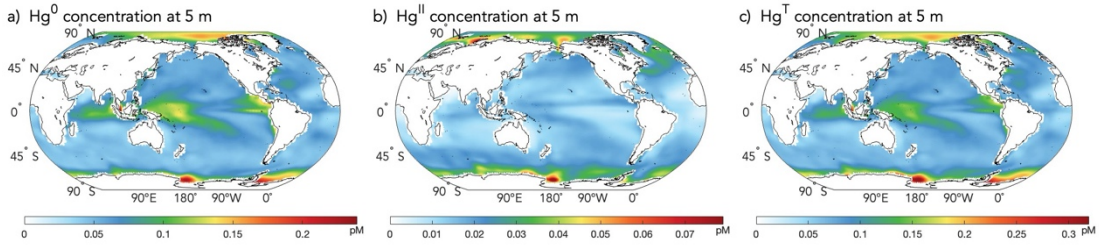

Figure 17: Spatial distributions of a) Hg0, b) HgII, and c) HgT concentrations at 5 m under the new redox rate settings

These changes lead to weaker net reduction at the surface (0–50 m), lowering fluxes to 8.22 Mg yr^{-1}. Hg^0 evasion slightly increased from 4.43 to 4.86 Mg yr^{-1}. The most pronounced changes occur in the surface ocean. At 5m, Hg^{II} concentrations decrease substantially, while Hg^0 concentrations approximately double. This leads to a 10% increase in the air–sea evasion flux of elemental mercury. Meanwhile, total mercury concentrations in the surface ocean decline markedly, although deep-ocean total mercury remains largely consistent with the baseline simulation. In the mid-depth ocean, net reduction declined from 3.62 to 1.53 Mg yr^{-1}. However, in the deep ocean (>1000 m), net reduction increased from 1.11 to 3.69 Mg yr^{-1}, likely due to the extended residence time of Hg and reduced oxidation rates.

https://doi.org/10.5194/egusphere-2025-3880
Preprint. Discussion started: 15 December 2025

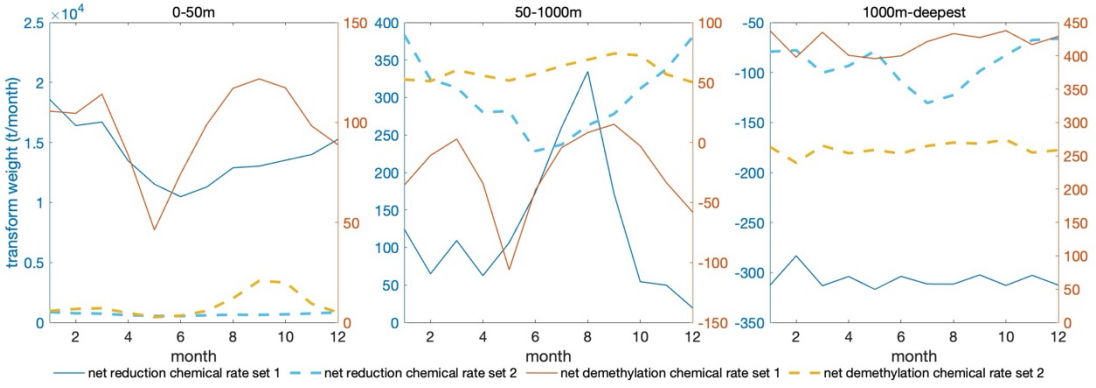

Figure 18: Monthly net transformation weight under two chemical rate scenarios, for: 0–50 m (left), 50–1000 m (center), and 1000 m to the deepest ocean layer (right). Set 1 (solid lines): the default reaction rates used in this model; Set 2 (dashed lines): reduced photochemical reaction rates following Bieser et al. (2023).

The monthly variability of net transformations (Fig. 18) further illustrates this vertical redistribution. In surface waters, the seasonal cycle of net reduction decreases, while demethylation maintains a weak late-summer peak. In the subsurface layer, redox direction reverses under the new rates, with net oxidation dominating for much of the year. In contrast, deep-ocean reactions remain to be oxidation and demethylation, with only the values decreasing.

5 Conclusion

We have developed a new global ocean mercury model, POP2/Hg v1.0, by embedding a mercury cycling module into the ocean component POP2 of the Community Earth System Model version 2 (CESM2) and coupling it with the Marine Biogeochemistry Library (MARBL). POP2/Hg v1.0 represents an advancement in marine mercury modelling by explicitly simulating redox transformations, air–sea exchange, particle partitioning, and the biologically driven vertical transport of mercury species in soft and hard forms. The model resolves major mercury forms, including Hg^0, Hg^{II}, Hg^p, and methylated mercury species (MMHg and DMHg), and links their behavior to ecosystem dynamics through MARBL's prognostic treatment of soft and hard POC. By integrating microbial methylation in subsurface remineralization zones and allowing for depth-resolved demethylation, the model captures measured MeHg distributions, particularly in oxygen-deficient waters, where previous models often lacked resolution or mechanistic representation.

The model largely reproduces the large-scale spatial patterns of Hg^0 and Hg^T observed in surface ocean datasets compiled by (Zhang et al., 2020). Simulation results show that the global Hg^0 production flux is 1.53×10^5 t yr^{-1} with a net evasion flux of approximately 4.5×10^3 t yr^{-1}. Subsurface layers serve as active zones of methylation and demethylation, with annual deep-ocean MMHg demethylation exceeding 3.4×10^3 t yr^{-1}. Hg^{II} accumulates in intermediate and deep waters due to particle

https://doi.org/10.5194/egusphere-2025-3880
Preprint. Discussion started: 15 December 2025

scavenging, with vertical gradients maintained by redox transformations and remineralization dynamics. These results emphasize the importance of the biological pump and microbial processes in shaping the oceanic mercury cycle.

Compared to prior global mercury models such as MITgcm-Hg and MERCY v2.0, POP2/Hg v1.0 offers improved coupling of Hg chemistry with ocean biogeochemistry, dynamic air–sea exchange, and a fully prognostic ecosystem framework. Future model development will focus on a fully coupled CESM2-Hg Earth system model including the atmosphere, land, and ocean, advancing our understanding of mercury behavior in the global ocean and its implications for ecological and human health.

Data and code availability

The POP2/Hg v1.0 model source code (Mao and Zhang, 2025) is archived on Zenodo at https://doi.org/10.5281/zenodo.17766499. The code deposit includes the full POP2/Hg v1.0 implementation, configuration files, and a technical documentation file required to reproduce all simulations presented in this study.

The Hg module is implemented within CESM2.1.3, which is distributed by NCAR under an open-source license. Access to the CESM source code is required to compile and run POP2/Hg v1.0 and is available at https://github.com/ESCOMP/cesm.

The forcing and observational datasets used for model evaluation are publicly accessible from the respective data providers as cited in Sect. 2.4. The model output generated in this study is not publicly archived due to file size limitations. However, all simulations can be fully reproduced using the open-source POP2/Hg v1.0 code, CESM2.1.3 configuration files. Model output is also available from the corresponding author upon reasonable request.

Author contributions

MM developed the POP2/Hg v1.0 model and drafted the manuscript. MM performed the simulations with help from YW and PZ. YZ contributed to model design, interpretation of results, and manuscript revision. LL, SH helped with the collection of data.

Competing interests

The authors declare that they have no conflict of interest.

Acknowledgements

We acknowledge the Louisiana Optical Network Infrastructure (LONI) for providing the high-performance computing resources used in this study. Simulations with CESM2 and POP2/Hg v1.0 were performed on LONI's QB-4 and associated HPC systems, and we thank the LONI staff for their technical support and maintenance of the computational environment.

https://doi.org/10.5194/egusphere-2025-3880
Preprint. Discussion started: 15 December 2025

References

Bieser, J., Amptmeijer, D.J., Daewel, U., Kuss, J., Soerensen, A.L., Schrum, C., 2023. The 3D biogeochemical marine mercury cycling model MERCY v2.0 – linking atmospheric Hg to methylmercury in fish. Geosci. Model Dev. 16, 2649–2688. https://doi.org/10.5194/gmd-16-2649-2023

Black, F.J., Conaway, C.H., Flegal, A.R., 2009. Stability of dimethyl mercury in seawater and its conversion to monomethyl mercury. Environ. Sci. Technol. 43, 4056–4062. https://doi.org/10.1021/es9001218

Chen, Q., Wu, Q., Cui, Y., Wang, S., 2025. Global seafood production practices and trade patterns contribute to disparities in exposure to methylmercury. Nat. Food 6, 491–502. https://doi.org/10.1038/s43016-025-01136-9

Dutay, J. C., Bullister, J. L., Doney, S. C., Orr, J. C., Najjar, R., Caldeira, K., Campin, J. M., Drange, H., Follows, M., Gao, Y., Gruber, N., Hecht, M. W., Ishida, A., Joos, F., Lindsay, K., Madec, G., Maier-Reimer, E., Marshall, J.C ., Matear, R. J., Monfray, P., Mouchet, A., Plattner, G. K., Sarmiento, J., Schlitzer, R., Slater, R., Totterdell, I. J., Weirig, M. F., Yamanaka, Y., Yool, A., 2002. Evaluation of ocean model ventilation with CFC-11: comparison of 13 global ocean models. Ocean Model. 4, 89–120. https://doi.org/10.1016/S1463-5003(01)00013-0

Kalinchuk, V. V., Lopatnikov, E. A., Astakhov, A. S., Ivanov, M. V., Hu, L., 2021. Distribution of atmospheric gaseous elemental mercury (Hg(0)) from the Sea of Japan to the Arctic, and Hg(0) evasion fluxes in the Eastern Arctic Seas: Results from a joint Russian-Chinese cruise in fall 2018. Sci. Total Environ. 753, 142003. https://doi.org/10.1016/j.scitotenv.2020.142003

Kuss, J., Zülicke, C., Pohl, C., Schneider, B., 2011. Atlantic mercury emission determined from continuous analysis of the elemental mercury sea-air concentration difference within transects between 50°N and 50°S. Glob. Biogeochem. Cycles 25. https://doi.org/10.1029/2010GB003998

Long, M. C., Moore, J. K., Lindsay, K., Levy, M., Doney, S. C., Luo, J. Y., Krumhardt, K. M., Letscher, R. T., Grover, M., Sylvester, Z. T., 2021. Simulations With the Marine Biogeochemistry Library (MARBL). J. Adv. Model. Earth Syst. 13, e2021MS002647. https://doi.org/10.1029/2021MS002647

Mason, R. P., Fitzgerald, W. F., Morel, F. M. M., 1994. The biogeochemical cycling of elemental mercury: Anthropogenic influences. Geochim. Cosmochim. Acta 58, 3191–3198. https://doi.org/10.1016/0016-7037(94)90046-9

Moore, J. K., Doney, S. C., Kleypas, J. A., Glover, D. M., Fung, I. Y., 2001. An intermediate complexity marine ecosystem model for the global domain. Deep Sea Res. Part II Top. Stud. Oceanogr., The US JGOFS Synthesis and Modeling Project: Phase 1 49, 403–462. https://doi.org/10.1016/S0967-0645(01)00108-4

Moore, J. K., Doney, S. C., Lindsay, K., 2004. Upper ocean ecosystem dynamics and iron cycling in a global three-dimensional model: GLOBAL ECOSYSTEM-BIOGEOCHEMICAL MODEL. Glob. Biogeochem. Cycles 18, n/a-n/a. https://doi.org/10.1029/2004GB002220

Morel, F. M. M., Kraepiel, A. M. L., Amyot, M., 1998. THE CHEMICAL CYCLE AND BIOACCUMULATION OF MERCURY. Annu. Rev. Ecol. Syst. 29, 543–566. https://doi.org/10.1146/annurev.ecolsys.29.1.543

https://doi.org/10.5194/egusphere-2025-3880
Preprint. Discussion started: 15 December 2025

Nerentorp Mastromonaco, M.G., Gårdfeldt, K., Langer, S., 2017. Mercury flux over West Antarctic Seas during winter, spring and summer. Mar. Chem., The role of oceans in the global mercury observing systems 193, 44–54. https://doi.org/10.1016/j.marchem.2016.08.005

Peng, D., Tan, Z., Yuan, T., Wu, P., Song, Z., Zhang, P., Huang, S., Zhang, Y., Lei, T., Middleton, B. A., Sonke, J. E., Lei, G., Gao, J., 2025. Human perturbations to mercury in global rivers. Sci. Adv. 11, eadw0471. https://doi.org/10.1126/sciadv.adw0471

Smith, R., Jones, P., Briegleb, B. P., Bryan, F. O., Danabasoglu, G., Dennis, J. M., Dukowicz, J., Eden, C., Fox-Kemper, B., Gent, P. R., Hecht, M., Jayne, S., Jochum, M., Large, W.G., Lindsay, K., Maltrud, M., Norton, N. J., Peacock, S. L., Vertenstein, M., Yeager, S., 2010. The Parallel Ocean Program (POP) reference manual: Ocean component of the Community Climate System Model (CCSM), NCAR Report.

Soerensen, A. L., Mason, R. P., Balcom, P.H., Jacob, D. J., Zhang, Y., Kuss, J., Sunderland, E. M., 2014. Elemental Mercury Concentrations and Fluxes in the Tropical Atmosphere and Ocean. Environ. Sci. Technol. 48, 11312–11319. https://doi.org/10.1021/es503109p

Soerensen, A. L., Mason, R. P., Balcom, P. H., Sunderland, E. M., 2013. Drivers of Surface Ocean Mercury Concentrations and Air–Sea Exchange in the West Atlantic Ocean. Environ. Sci. Technol. 47, 7757–7765. https://doi.org/10.1021/es401354q

Soerensen, A. L., Sunderland, E. M., Holmes, C. D., Jacob, D. J., Yantosca, R. M., Skov, H., Christensen, J. H., Strode, S. A., Mason, R. P., 2010. An Improved Global Model for Air-Sea Exchange of Mercury: High Concentrations over the North Atlantic. Environ. Sci. Technol. 44, 8574–8580. https://doi.org/10.1021/es102032g

Strode, S., Jaeglé, L., Emerson, S., 2010. Vertical transport of anthropogenic mercury in the ocean: OCEAN MERCURY TRANSPORT. Glob. Biogeochem. Cycles 24, n/a-n/a. https://doi.org/10.1029/2009GB003728

Sunderland, E. M., Mason, R. P., 2007. Human impacts on open ocean mercury concentrations: OPEN OCEAN MERCURY MODEL. Glob. Biogeochem. Cycles 21, n/a-n/a. https://doi.org/10.1029/2006GB002876

Wang, J., Xie, Z., Wang, F., Kang, H., 2017. Gaseous elemental mercury in the marine boundary layer and air-sea flux in the Southern Ocean in austral summer. Sci. Total Environ. 603–604, 510–518. https://doi.org/10.1016/j.scitotenv.2017.06.120

Wang, Y., Wu, P., Zhang, Y., 2023. Climate-driven changes of global marine mercury cycles in 2100. Proc. Natl. Acad. Sci. 120, e2202488120. https://doi.org/10.1073/pnas.2202488120

Yuan, T., Zhang, P., Song, Z., Huang, S., Wang, X., Zhang, Y., 2023. Buffering effect of global vegetation on the air-land exchange of mercury: Insights from a novel terrestrial mercury model based on CESM2-CLM5. Environ. Int. 174, 107904. https://doi.org/10.1016/j.envint.2023.107904

Zhang, P., Zhang, Y., 2022. Earth system modeling of mercury using CESM2 – Part 1: Atmospheric model CAM6-Chem/Hg v1.0. Geosci. Model Dev. 15, 3587–3601. https://doi.org/10.5194/gmd-15-3587-2022

Zhang, Y., Jacob, D. J., Dutkiewicz, S., Amos, H. M., Long, M. S., Sunderland, E. M., 2015. Biogeochemical drivers of the fate of riverine mercury discharged to the global and Arctic oceans: RIVER MERCURY IN THE OCEAN. Glob. Biogeochem. Cycles 29, 854–864. https://doi.org/10.1002/2015GB005124

https://doi.org/10.5194/egusphere-2025-3880
Preprint. Discussion started: 15 December 2025

Zhang, Y., Jaeglé, L., Thompson, L., 2014a. Natural biogeochemical cycle of mercury in a global three-dimensional ocean tracer model. Glob. Biogeochem. Cycles 28, 553–570. https://doi.org/10.1002/2014GB004814

Zhang, Y., Jaeglé, L., Thompson, L., Streets, D.G., 2014b. Six centuries of changing oceanic mercury: Anthropogenic mercury in ocean. Glob. Biogeochem. Cycles 28, 1251–1261. https://doi.org/10.1002/2014GB004939

Zhang, Y., Soerensen, A. L., Schartup, A. T., Sunderland, E.M., 2020. A Global Model for Methylmercury Formation and Uptake at the Base of Marine Food Webs. Glob. Biogeochem. Cycles 34, e2019GB006348. https://doi.org/10.1029/2019GB006348

Zhang, Y., Song, Z., Huang, S., Zhang, P., Peng, Y., Wu, P., Gu, J., Dutkiewicz, S., Zhang, H., Wu, S., Wang, F., Chen, L., Wang, S., Li, P., 2021. Global health effects of future atmospheric mercury emissions. Nat. Commun. 12, 3035. https://doi.org/10.1038/s41467-021-23391-7